Supporting Information for

# Thermally Responsive Architected Actuators with Programmable Shape Morphing and Tunable Stiffness

**This PDF file includes:**

Figs. S1 to S8
Tables S1

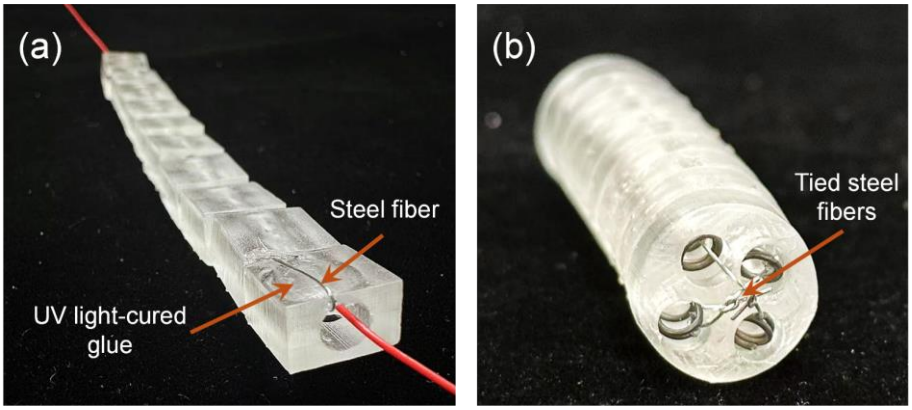



Figure S1. Two types of boundary constraints applied to TSAMS for the morphing process. (a) Steel fibers and UV light-cured glue for single-layer units. (b) Bundle steel fibers together for the multi-layer units.

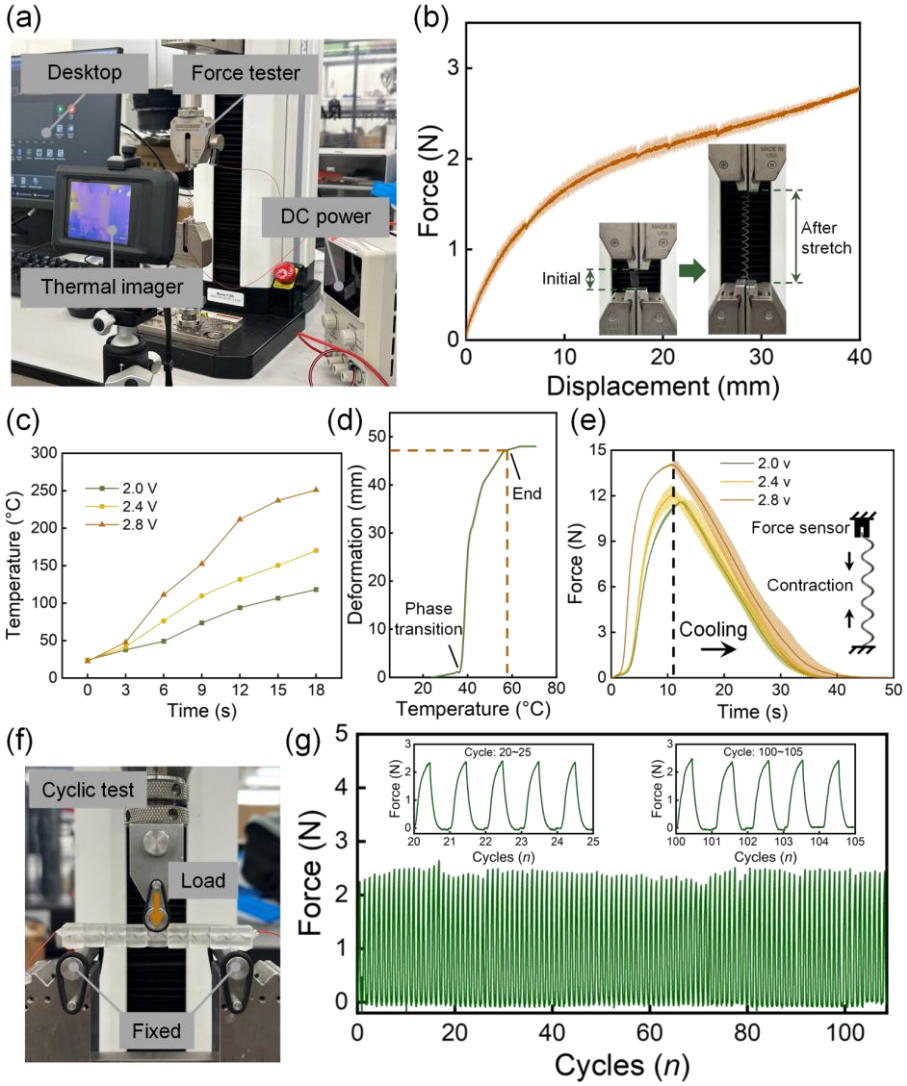



Figure S2. Electro-thermo-mechanical characterization of SMA springs and beam-shaped TSAMS. (a) Experimental setup for tensile tests of unactuated SMA springs to evaluate mechanical strength. (b) Force-displacement curves from tensile tests of an unactuated SMA spring. Colored lines represent average values, and shaded areas denote standard deviations from three independent tests. (c) Temperature response of an SMA spring under various actuation voltages. (d) Deformation of an SMA spring with increasing temperature. (e) Contracting force of an SMA spring over time under different actuation voltages. Colored lines represent average values, and shaded areas denote standard deviations from three independent tests. (f) Experimental setup for cyclic three-point bending tests of beam-shaped TSAMS to evaluate mechanical durability across repeated actuation cycles. (g) Force measured over 105 actuation cycles from cyclic three-point bending tests.

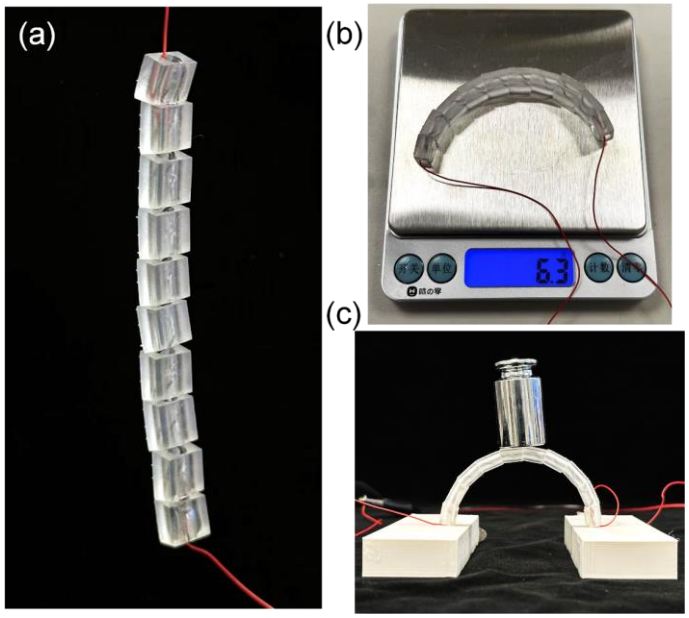



Figure S3. A 6.3 g TSAMS unit morphs from a flat configuration into a 180° arc under electrothermal actuation and supports a 100 g load, which is more than 15.8 times its own weight. (a) The initial flat shape of TSAMS. (b) The weight of the TSAMS unit. (C) The morphing and load bearing of the TSAMS unit.

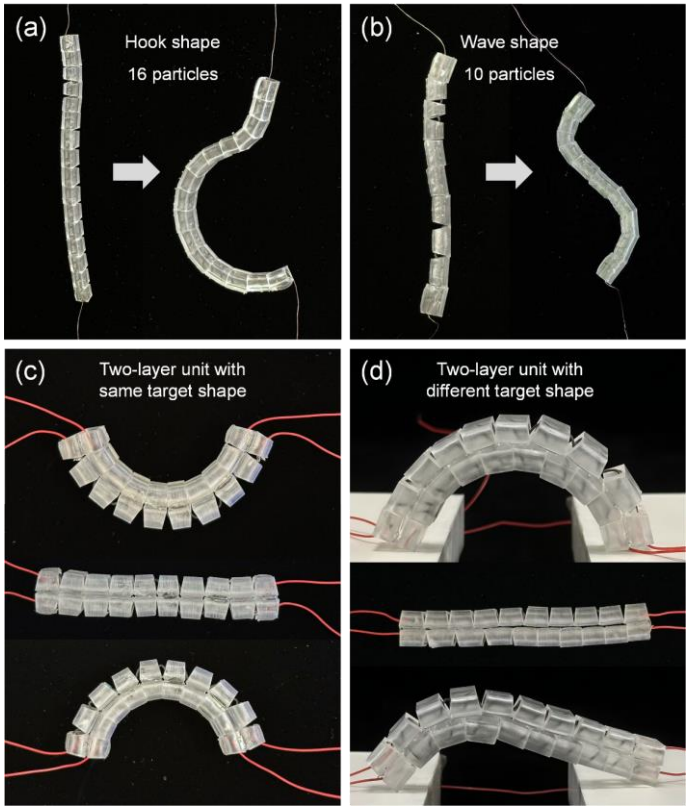



Figure S4. Experimental demonstration of the morphing ability of the TSAMS. The initial and morphed state of the TSAMS with (a) hook shape. (b) wave shape. (c) two identical layers. (d) two different layers.

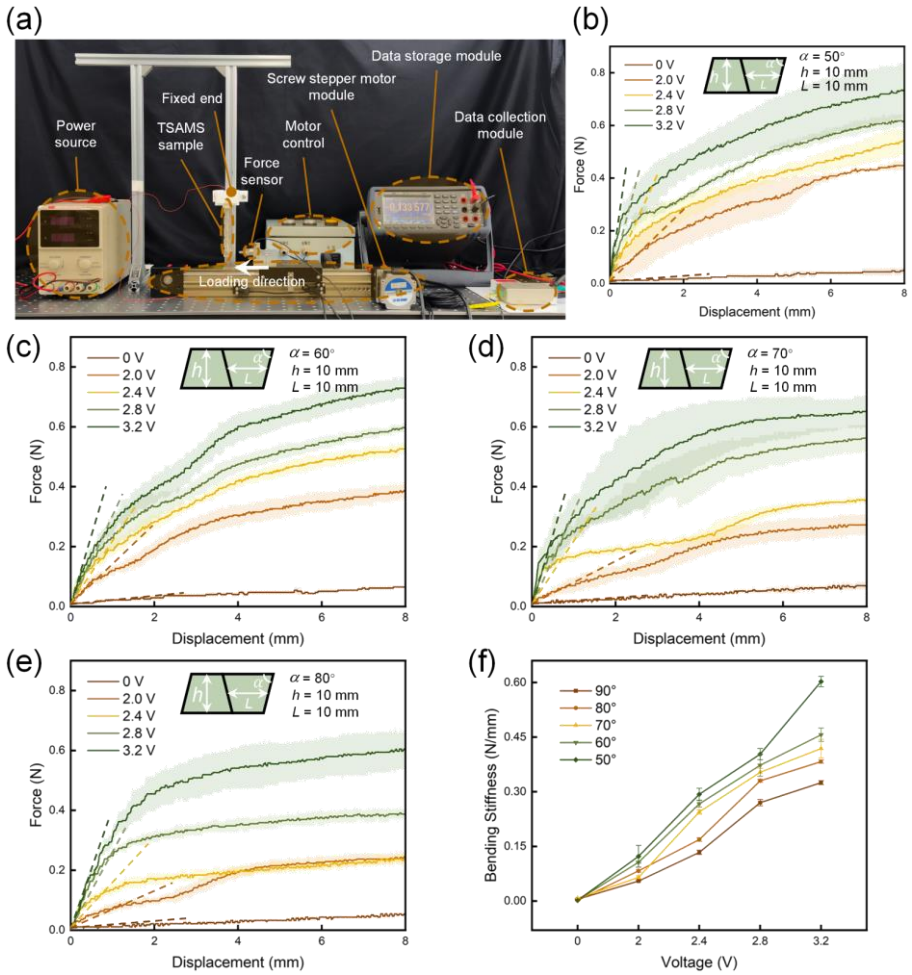



Figure S5. Cantilever bending tests of TSAMS with various inclined angles. (a) Experimental setup. (b-e) Force-displacement curves for TSAMS with 50°, 60°, 70°, and 80° inclined angles at various actuating voltages. Colored lines represent average values, and shaded areas denote standard deviations from three independent tests. (f) Comparison of the bending stiffness of TSAMS with different inclined angles under actuating voltages ranging from 0 to 3.2 V. Colored lines represent average values, and error bars denote standard deviations from three independent tests.

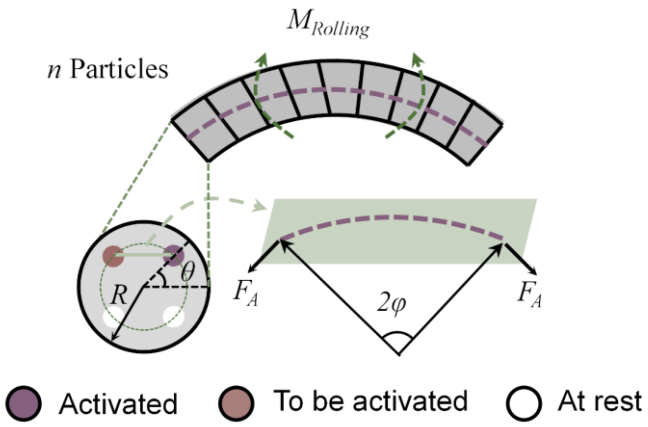



Figure S6. Illustration of the theoretical model for the rolling motion of the concentric robot.

*The theoretical model for the rolling motion:* we consider the robot body as a curved arc with angular coordinate $\theta$ defined along its contour, where $\theta = 0$ corresponds to the inner side of the C-bend. When a contraction is applied at $\theta = 0$, the actuating SMA spring undergoes isotonic contraction with a strain of $\Delta\varepsilon$. This results in a local reduction in axial strain, such that the strain at $\theta = 0$ becomes:

$$\varepsilon_0 = \varepsilon - \Delta\varepsilon$$

where $\varepsilon$ is the baseline strain. The strain then linearly redistributes along the arc, reaching $\varepsilon$ at $\theta = \pi/2$ and increasing to $\varepsilon_\pi = \varepsilon + \Delta\varepsilon$ at $\theta = \pi$ (the outer side of the C-bend). When the axial muscle at $\theta = 0$ becomes inactive, the body begins to recover from its bent configuration. To sustain or initiate rolling, adjacent actuators at $\theta \neq 0$ must be activated. The activated SMA spring generates a contraction force $\vec{F}_A$, which, when applied at an off-centered location along the arc, induces a moment at the center of mass as $\sum \vec{r} \times \vec{F}_A$, where $\vec{r}$ is the vector between the center of curvature and the axial muscle force. The rolling moment can be expressed as:

$$\vec{M}_{Rolling} = -2F_A R \sin\varphi \sin\theta \vec{e}_z$$

Therefore, the sign of $\theta$ governs the progression of the SMA spring actuation, and thereby the rolling direction. If actuation occurs in the upper region ($0 < \theta < \pi/2$), the generated moment drives rolling toward the opening direction of the C-bend. Conversely, if actuation occurs in the lower region ($-\pi/2 < \theta < 0$), the body rolls in the opposite direction, still progressing toward the opening side of the bend. The model can be further extended to analyze segmented structures, such as the proposed self-rolling robot. Assuming the robot consists of $n$ identical particles, the net moment about the center of the local cross-section can be expressed as:

$$M^n_{Rolling} = -2F_A R \sin\frac{\varphi}{n} \sin\theta$$

The total torque $M_{Rolling} = nM^n_{Rolling}$.

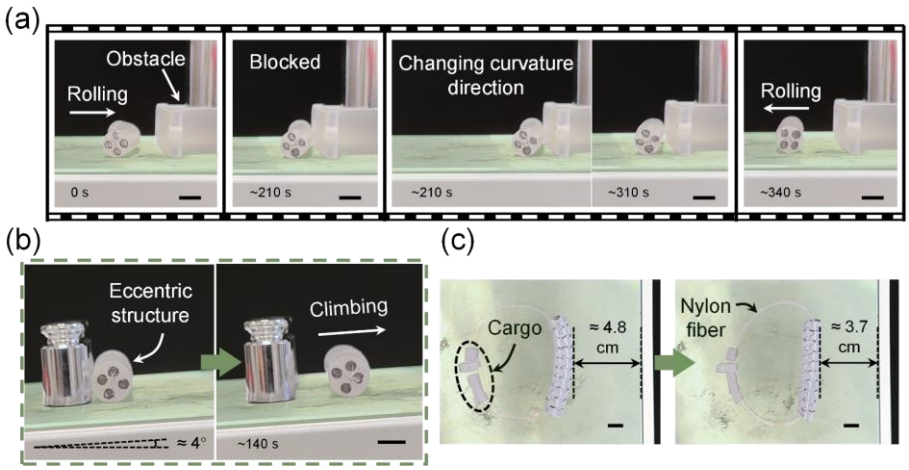



Figure S7. Additional locomotion scenarios of the untethered thermal-driven self-rolling robots. (a) Autonomous alteration of body curvature and reversal of rolling direction upon encountering obstacles. (b) The eccentric robot climbs slope up to 4 degrees. (c) Rolling robot transporting a cargo equivalent to 25% of its body weight.

*Additional locomotion scenarios of the rolling robots:* Figure S7a illustrates the robots' capability to autonomously adjust their body curvature and reverse rolling direction when encountering obstacles. In the initial stage, the pre-bent robot's body curvature facilitates rightward rolling on the heating plate. Upon encountering an obstacle, the SMA spring on the right side is heated by contacting the obstacle, gradually changing the opening of the C-bend from the left to the right, adopting a reversed body curvature. This change prompts the robot to roll leftward, driven by the new curvature. A similar reversal behavior is observed in the eccentric-designed robot, as demonstrated in Movie S2. This intrinsic ability to adapt and interact with the environment is particularly advantageous for navigating and exploring unfamiliar terrains, such as those encountered in outer space. To further demonstrate the locomotion capabilities of the rolling robots in environmental exploration, we conduct slope-climbing tests for both the concentric- and eccentric-designed robots, as shown in Figure 3e, Figure S7b and Movie S3. The results indicate that the concentric-designed robot can continuously roll up a 7-degree slope, whereas the eccentric-designed robot can only overcome a 4-degree slope. This difference arises because the initial bending of the concentric-designed robot stabilizes its position on the slope, whereas the absence of such bending in the eccentric-designed robot causes it to roll back to its starting position immediately after attempting to ascend.

In addition to mobility, cargo transportation is a significant application for untethered robots [1]. Using an SLA printer, we fabricate irregularly shaped particles of varying sizes to serve as cargo and connect them to the rolling robot using nylon fibers, as illustrated in Figure S7c. The experiments demonstrate that the robot can overcome the frictional force between the cargo and the heating plate, maintaining a constant speed in the designed direction (Movie S4). The maximum cargo weight that the robot can transport is inherently linked to its size, with the capacity increasing as the robot is scaled up. These results highlight the suitability of the proposed self-rolling robot for cargo transportation tasks.

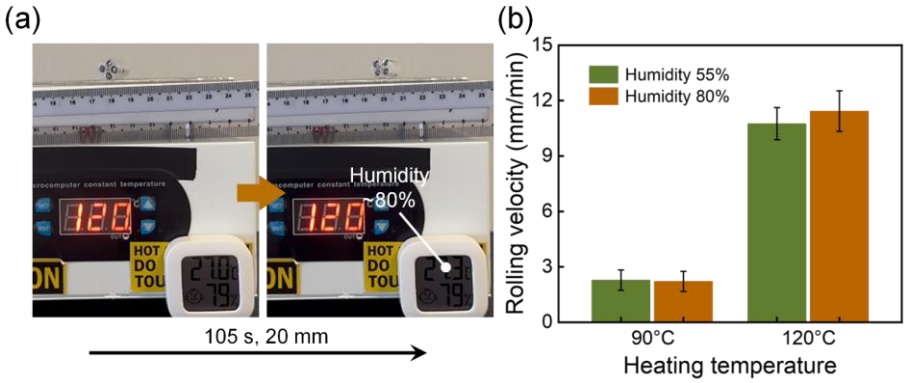



Figure S8. Environmental robustness test of the concentric rolling robot. (a) Experimental setup under high-humidity conditions (~80%) using a humidity meter. (b) Comparison of rolling speed with different heating temperatures under different humidity levels. Colored bars represent average values, and error bars denote standard deviations from three independent tests.

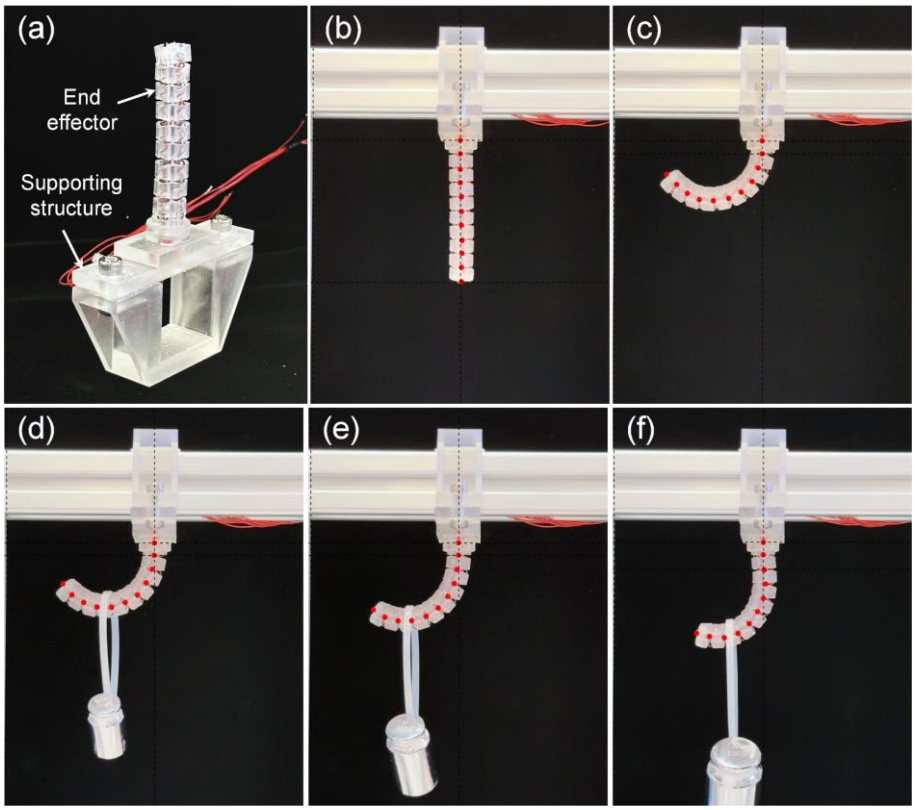



Figure S9. Load-bearing tests for the soft manipulator. (a) Experimental setup. (b) The initial state of the end effector before applying any load. (c-f) Comparison of the morphed shapes of the end effector under varying loads: 0 g, 50 g, 100 g, and 250 g.

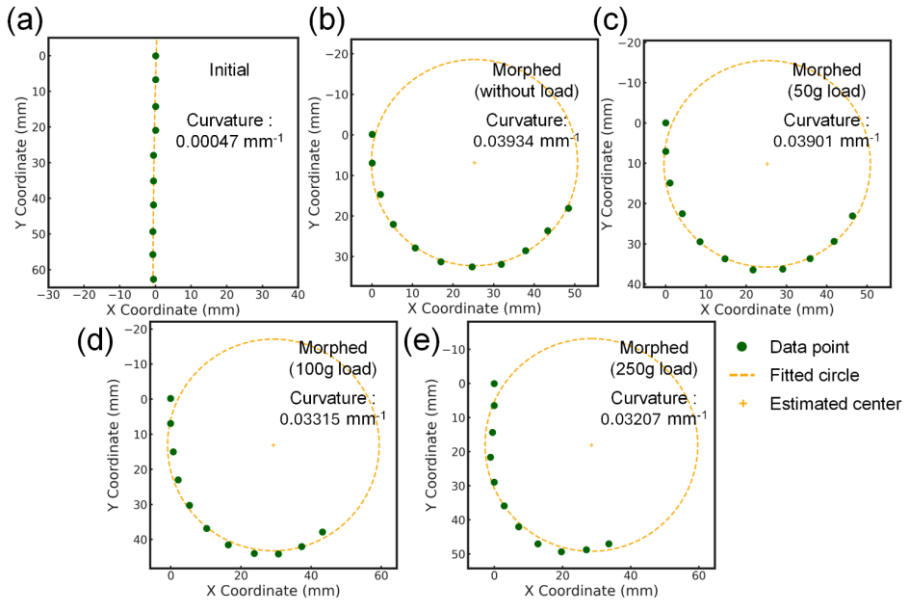



Figure S10. Comparison of the curvature of the end effector under various loading conditions. (a) Unactuated state. (b) Morphed shape without external load. (c) Morphed shape under a 50 g load. (d) Morphed shape under a 100 g load. (e) Morphed shape under a 250 g load.

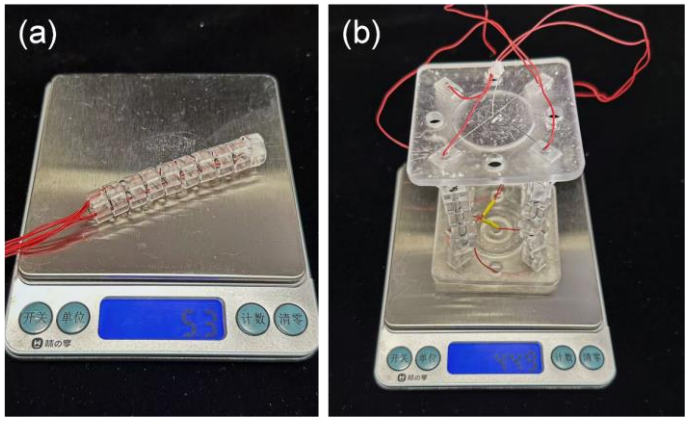



Figure S11. Weight measurements of the soft manipulator components. (a) The end effector, weighing 5.3 g. (b) The twisting base, weighing 44.9 g.

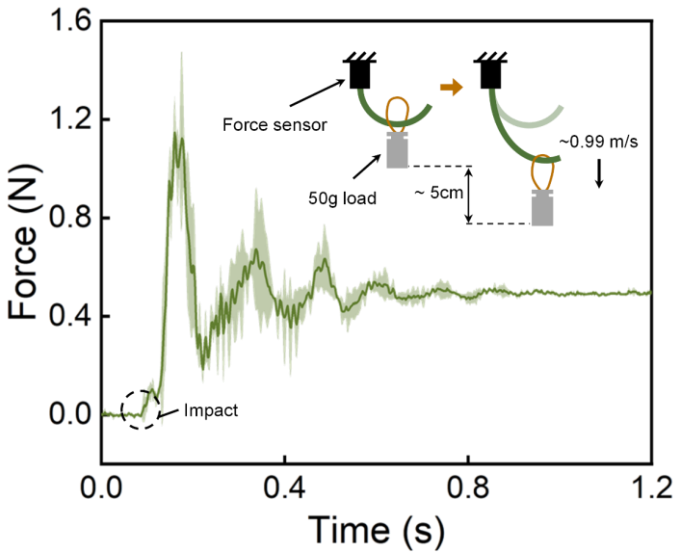



Figure S12. Dynamic load-bearing test of the soft manipulator. Colored lines represent average values, and shaded areas denote standard deviations from three independent tests.

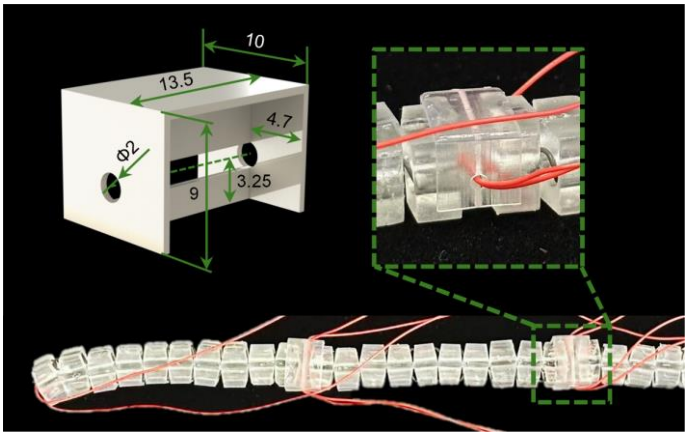



Figure S13. The design and experimental demonstration of connecting joints in the snake-inspired robot. Unit, mm.

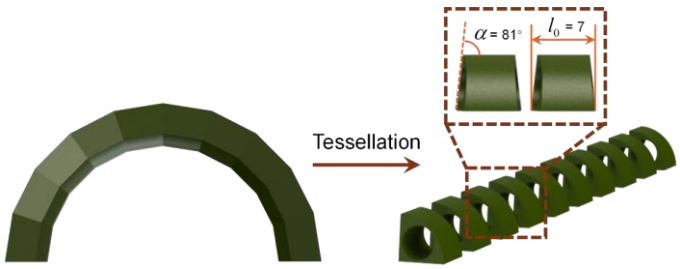



Figure S14. The geometry design of one TSAMS unit in the self-rolling robot. Unit, mm.

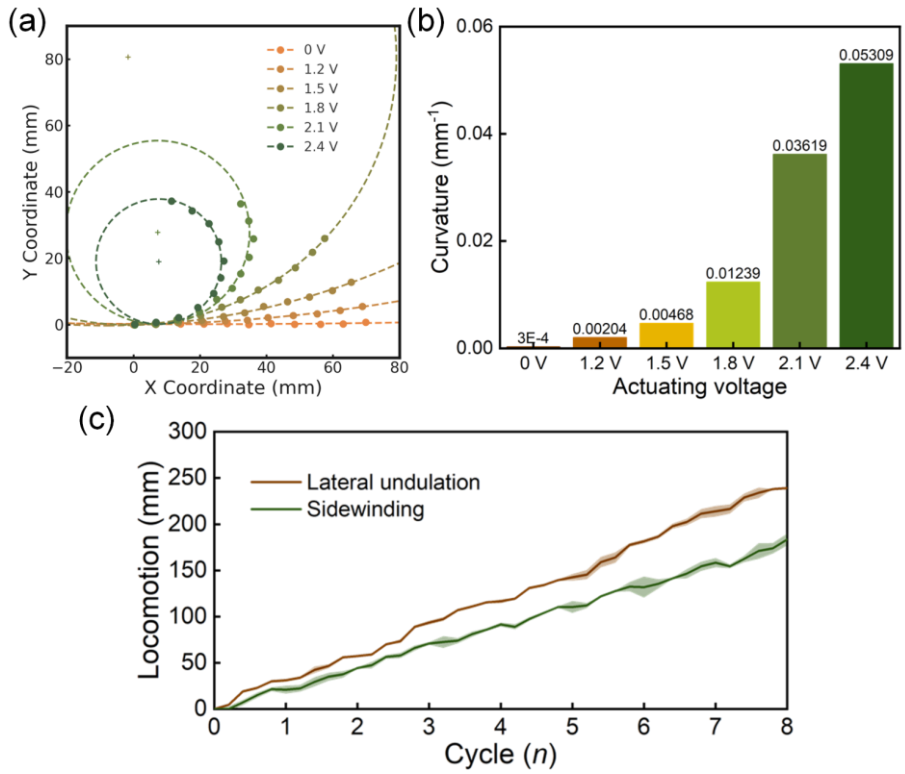



Figure S15. Characterization of the snake-inspired robot. (a) Shape morphing of a single segment under different actuating voltages. (b) Comparison of the resulting curvature at each voltage level. (c) Locomotion speed measurements under sidewinding and lateral undulation modes. Colored lines represent average values, and shaded areas denote standard deviations from two independent tests.

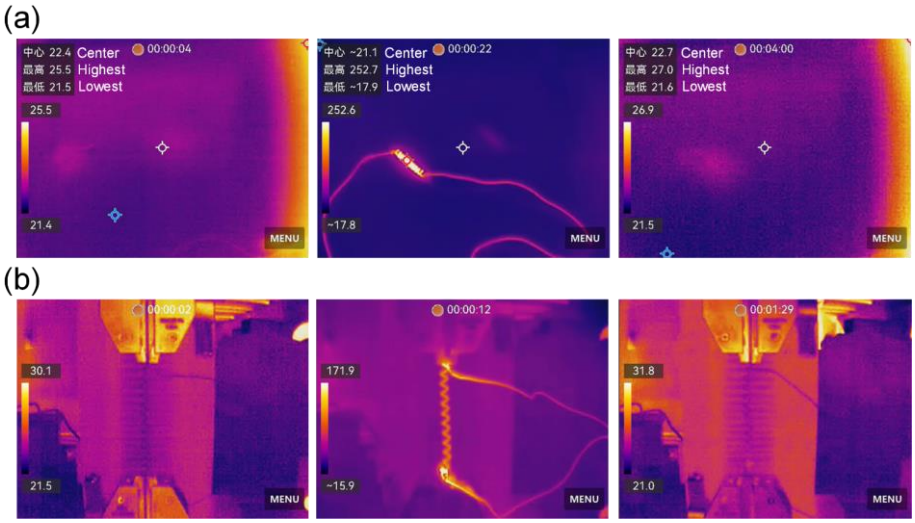



Figure S16. Infrared thermal image of the SMA heating and cooling process. (a) Deformation tests of SMA springs. (b) Contracting force measurements of SMA springs.

Table S1. Mechanical Properties and Post-Curing Conditions of SLA-Printed Particles [2]

| Structure | Materials | Ultimate Tensile Strength | Tensile Modulus | Flexural Modulus | Elongation at Break | Heat Deflection Temp.(0.45 MPa) | Post-curing |
|---|---|---|---|---|---|---|---|
| SLA-printed particles | Clear Resin V4 (Formlabs) | 65.0 MPa | 2.8 GPa | 2.2 GPa | 6% | 73 °C | 15 min, 60°C |

Table S2. Comparison of shape morphing and stiffness tuning performance between TSAMS and other prototypes

| Reference | Actuation mode | Stiffness variation ratio | Integrated shape morphing and stiffness tuning | Response time |
|---|---|---|---|---|
| [3] | Fluidic-driven (positive pressure) | 3 | Yes | NA |
| [4] | Fluidic-driven (positive pressure) | 5 | Yes | 2.5-5 s |
| [5] | Fluidic-driven (positive pressure) | 5 | Yes | 620 ms |
| [6] | Fluidic-driven (positive pressure) | 3 | Yes | 1.15-1.97 s (stiffness), 0.56-1.89 s (morphing) |
| [7] | Electrical field-driven | 100 | Yes | <1 s (4.7 kV) |
| [8] | Osmolyte concentration (electrosorption) | 6 | Yes | 1 h |
| [9] | Thermal-driven | 5.1 | Yes | 30 s (heating) + 90 s (cooling) |
| [10] | Thermal-driven | 130 | No | The morphing drone: ~1 min (heating), ~7 min (cooling) |
| [11] | Thermal-driven | 24.7 | No | 2 s (150 V), 4 s (100 V) |
| [12] | Thermal and electrical field-driven | 90 | No | 30 s |
| [13] | Magnetic field-driven | 1.35 | No | NA |
| [14] | NIR light-driven | 12.96 (10 mM $Ca^{2+}$ initial) | No | 180 s |
| [15] | Multistable and electromagnetic-driven | 8 (bending), 27 (twisting) | Yes | ~125s |
| **This work** | **Thermal-driven** | **308** | **Yes** | **~1 s (5 V), ~ 2.5 s (3.2 V)** |

# References


1. Zhai, F., et al., *4D-printed untethered self-propelling soft robot with tactile perception: Rolling, racing, and exploring.* Matter, 2021. **4**(10): p. 3313-3326.
2. Formlabs, *Clear Resin V4 Technical Data Sheet*. 2023, Formlabs, Inc.: Somerville, MA.
3. Mahadevan, K., et al., *3D knit pneumatic actuators for wearable haptic displays.* Extreme Mechanics Letters, 2023. **65**: p. 102102.
4. Zhu, M., et al., *Fluidic fabric muscle sheets for wearable and soft robotics.* Soft robotics, 2020. **7**(2): p. 179-197.
5. Zhang, Z., et al., *Soft and lightweight fabric enables powerful and high-range pneumatic actuation.* Science Advances, 2023. **9**(15): p. eadg1203.
6. Fei, Y., J. Wang, and W. Pang, *A novel fabric-based versatile and stiffness-tunable soft gripper integrating soft pneumatic fingers and wrist.* Soft robotics, 2019. **6**(1): p. 1-20.
7. Cacucciolo, V., et al., *Stretchable pumps for soft machines.* Nature, 2019. **572**(7770): p. 516-519.
8. Must, I., E. Sinibaldi, and B. Mazzolai, *A variable-stiffness tendril-like soft robot based on reversible osmotic actuation.* Nature communications, 2019. **10**(1): p. 344.
9. Yuen, M.C., R.A. Bilodeau, and R.K. Kramer, *Active variable stiffness fibers for multifunctional robotic fabrics.* IEEE Robotics and Automation Letters, 2016. **1**(2): p. 708-715.
10. Hwang, D., et al., *Shape morphing mechanical metamaterials through reversible plasticity.* Science robotics, 2022. **7**(63): p. eabg2171.
11. Shan, W., et al., *Rigidity-tuning conductive elastomer.* Smart Materials and Structures, 2015. **24**(6): p. 065001.
12. Shintake, J., et al. *Variable stiffness actuator for soft robotics using dielectric elastomer and low-melting-point alloy*. in *2015 IEEE/RSJ International Conference on Intelligent Robots and Systems (IROS)*. 2015. IEEE.
13. Varga, Z., G. Filipcsei, and M. Zrínyi, *Magnetic field sensitive functional elastomers with tuneable elastic modulus.* Polymer, 2006. **47**(1): p. 227-233.
14. Stowers, R.S., S.C. Allen, and L.J. Suggs, *Dynamic phototuning of 3D hydrogel stiffness.* Proceedings of the National Academy of Sciences, 2015. **112**(7): p. 1953-1958.
15. Aksoy, B. and H. Shea, *Multistable shape programming of variable-stiffness electromagnetic devices.* Science Advances, 2022. **8**(21): p. eabk0543.